Nanoscale



PAPER View Article Online
View Journal | View Issue



Cite this: Nanoscale, 2020, 12, 17886

Bidirectional tuning of phase transition properties in Pt: VO₂ nanocomposite thin films†

Zihao He,^a Jie Jian,^b Shikhar Misra,^b Xingyao Gao,^b Xuejing Wang,^b Zhimin Qi,^b Bo Yang,^b Di Zhang,^b Xinghang Zhang^b and Haiyan Wang (1) **a,b**

A phase transition material, VO₂, with a semiconductor-to-metal transition (SMT) near 341 K (68 °C) has attracted significant research interest because of drastic changes in its electrical resistivity and optical dielectric properties. To address its application needs at specific temperatures, tunable SMT temperatures are highly desired. In this work, effective transition temperature (T_c) tuning of VO₂ has been demonstrated via a novel Pt:VO₂ nanocomposite design, i.e., uniform Pt nanoparticles (NPs) embedded in the VO₂ matrix. Interestingly, a bidirectional tuning has been achieved, i.e., the transition temperature can be systematically tuned to as low as 329.16 K or as high as 360.74 K, with the average diameter of Pt NPs increasing from 1.56 to 4.26 nm. Optical properties, including transmittance (T%) and dielectric permittivity (e') were all effectively tuned accordingly. All Pt:VO₂ nanocomposite thin films maintain reasonable SMT properties, i.e. sharp phase transition and narrow width of thermal hysteresis. The bidirectional T_c tuning is attributed to two factors: the reconstruction of the band structure at the Pt:VO₂ interface and the change of the Pt:VO₂ phase boundary density. This demonstration sheds light on phase transition tuning of VO₂ at both room temperature and high temperature, which provides a promising approach for VO₂-based novel electronics and photonics operating under specific temperatures.

Received 25th May 2020, Accepted 29th July 2020 DOI: 10.1039/d0nr04008h

rsc.li/nanoscale

Introduction

Mott metal-insulator phase transition has been widely studied in metal oxides owing to abrupt changes in their physical properties during phase transition. Such changes arise due to the electron-electron interaction effect² and have potential applications in memory and switching devices.³ One such Mott transition material is vanadium dioxide (VO2), which has been the centerpiece of transition metal oxide research over the past decade because of its ultrafast and reversible phase transition at around 341 K.4-6 The room-temperature semiconductor phase VO₂ has a monoclinic crystal structure. By the reversible first-order semiconductor-to-metal transition (SMT), the monoclinic phase VO₂ transforms into a tetragonal rutile crystal structure.^{7,8} Such phase transition drastically changes its electrical and optical properties, with an electrical resistivity transition of 4-5 orders of magnitude and optical transmission transition of 40-50% in the near infrared and terahertz wavelength regions.¹⁰ The resulting functional property

It is attractive to tailor the phase transition temperature (T_c) of VO₂ thin films to satisfy a specific working temperature. Thus recent efforts have been devoted towards the realization of T_c tuning of VO_2 films for potential device applications. T_c tuning of VO₂ has mainly been achieved by doping and strain engineering. Specifically, by introducing different substrates and buffer layers, the T_c of VO_2 films can either be tuned up or down by the strain from the lattice misfit between the film and the substrate. 15-17 However, a large strain is usually accompanied by high defect densities. 18,19 Alternatively, a number of dopants, including Mg, W, Al, Cr, and Nb, were reported to successfully tune the transition temperature of VO2 films from 308 to 384 K.^{20–23} However, the increase of doping level could cause the degradation of phase transition properties due to consequent defects²⁴ and multivalent vanadium ions.25

Recently, a VO₂-metal nanocomposite design was proposed as a novel approach to overcome the abovementioned degradation. ^{26,27} Depending on the work function of different metals, the tunability of $T_{\rm c}$ could be achieved primarily by the alignment of the Fermi level of VO₂ and embedded metal nanoparticles (NPs). Au NPs were first introduced for $T_{\rm c}$ tuning

tuning allows a wide variety of applications involving optical and electrical based sensing and switching devices, including memristors, ¹¹ chemical and biological sensors, ¹² intelligent window coatings, ¹³ and switching materials. ¹⁴

^aSchool of Electrical and Computer Engineering, Purdue University, West Lafayette, IN 47907-2045, USA. E-mail: hwang00@purdue.edu

^bSchool of Materials Engineering, Purdue University, West Lafayette, IN 47907-2045, IISA

[†]Electronic supplementary information (ESI) available. See DOI: 10.1039/d0nr04008h

Nanoscale Paper

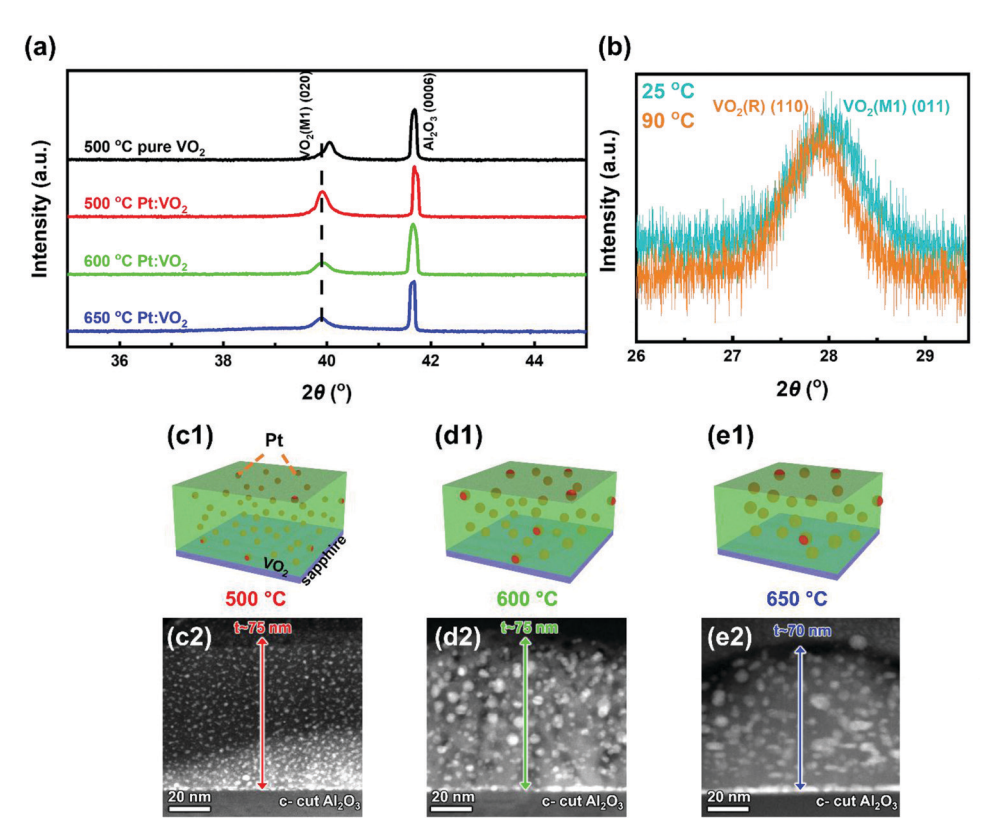


Fig. 1 (a) XRD θ -2 θ spectra of the pure VO₂ film and Pt: VO₂ nanocomposite thin films on c-cut sapphire substrates. (b) XRD ϕ -scans at 25 °C and 90 °C of 500 °C deposited Pt: VO2 nanocomposite thin films. (c1, d1, and e1) Schematic diagram of the temperature dependence of Pt: VO2 nanocomposite thin films grown on c-cut sapphire. Size control is possible through temperature control during pulsed laser deposition (PLD). (c2, d2, and e2) STEM cross-section images of the Pt: VO₂ nanocomposite thin films deposited at 500, 600, and 650 °C, respectively.

of VO₂ for room temperature applications.²⁶ SMT in Au: VO₂ nanocomposite films was tuned by charge-transfer-induced bandwidth control. The effective tuning of VO2 phase transition properties was later experimentally demonstrated using metals with different work functions, and a record low T_c of 301.8 K was achieved with high film quality and reasonable SMT performance.27

In this work, we propose to achieve effective T_c tuning of VO₂ films via a single metal selection, considering that the work function of many metal NPs is size dependent and thus can be used to tune the T_c of VO_2 . More specifically, a bidirectional T_c tuning of VO_2 films is proposed via a novel Pt: VO_2 nanocomposite design. As illustrated in Fig. 1, Pt NPs with various NP sizes are uniformly embedded in the VO2 matrix using a single-step pulsed laser deposition (PLD) method. Pt was selected due to its size dependent work function. Interestingly, the work function of Pt NPs can be either higher or lower than the work function of VO2 via size tuning. Therefore, the conduction band of VO2 can be bent either upwards or downwards for T_c tuning by forming a Schottky junction with the metal phase.5 The proposed NP size control can be realized via deposition temperature variation. Through NP size tuning, it is possible to achieve tunable phase transition properties and thus the transport properties, optical transmittance, dielectric permittivity, and epsilon-near-zero

(ENZ) wavelength of the samples were measured and correlated with the Pt: VO2 structures.

Experimental

Pt: VO₂ nanocomposite thin films were deposited onto c-cut sapphire substrates using pulsed laser deposition (PLD, KrF excimer laser, $\lambda = 248$ nm). The laser beam was incident at an angle of 45° to achieve an approximate energy density of 3 J cm⁻². The laser beam was aligned to maintain comparable Pt/V composition of all films deposited at different temperatures. A V2O5 target, which was pressed and sintered by the conventional method, was used for Pt:VO2 nanocomposite thin film deposition along with the Pt strip. All films were deposited at a constant oxygen pressure (0.01 Torr) and a laser frequency (2 Hz). The deposition temperatures ranged from 500 to 650 °C to control the size of Pt NPs.

The microstructures of Pt: VO2 thin films were characterized through X-ray diffraction (XRD, PANalytical Empyrean with Cu K_{α} radiation), selected-area electron diffraction (SAED), scanning transmission electron microscopy (STEM, Thermo Scientific Talos F200X), energy dispersive X-ray spectroscopy (EDS) and high resolution STEM (HR-STEM). The phase transition of Pt: VO₂ thin films was studied using in situ

Paper Nanoscale

high temperature XRD (PANalytical Empyrean with a DHS 1100 domed heating stage). The HR-STEM images in the highangle annular dark-field (HAADF) mode were acquired using a Thermo Scientific Themis Z with a Cs probe corrector operated at 200 kV. Cross-sectional TEM samples were prepared via a standard grinding procedure, involving manual grinding, polishing, dimpling, and a final ion-milling step (PIPS 695 precision ion polishing system, 5 keV). The composition of nanocomposite thin films was characterized by large-scale EDS quantification on a Quanta 600 scanning electron microscope (SEM). The electrical resistance of the nanocomposite thin films was investigated in a physical property measurement system (PPMS, Quantum Design DynaCool) at temperature ranging from 290 to 390 K. The dielectric permittivity of the as-deposited nanocomposite thin films was measured using an angular dependent spectroscopic ellipsometer (RC2 ellipsometer, J.A. Woollam) at three different angles of incidence (55°, 65°, and 75°), both at room temperature (25 °C) and elevated temperature (90 °C). Normal incident depolarized transmittance (T%) measurement of the as-deposited nanocomposite thin films was carried out on an optical spectrophotometer (PerkinElmer LAMBDA 1050 UV/Vis spectrophotometer).

Results and discussion

Fig. 1a compares the XRD θ -2 θ scans of Pt:VO₂ nanocomposite thin films on c-cut sapphire substrates deposited at three different temperatures: 500, 600, and 650 °C. All the samples show the presence of the VO₂ (M1) (020) peak, which suggests a highly textured b-axis growth of the VO2 matrix on c-cut sapphire. The peak positions of the VO₂ (M1) (020) peak in all Pt: VO2 films shift slightly to the left with respect to the pure VO₂ (M1) (020) peak. The result confirms the presence of monoclinic phase VO_2 in all Pt: VO_2 films. The VO_2 (011) ϕ scans of Pt: VO2 thin films (Fig. S1a and b, ESI†) show three sets of peaks with an in-between rotation of 60°. In contrast, no obvious peak was observed in the VO₂ (102) ϕ -scan. The ϕ scan results further support the VO₂ (M1) (020) out-of-plane growth on c-cut sapphire. However, the VO2 peak intensities decrease gradually at higher temperatures, which suggests lower film texture quality at higher temperatures. In addition, the XRD spectrum of the Pt: VO₂ film deposited at 650 °C shows an overlap between the Pt (111) peak and VO2 (M1) (020) peak, suggesting a (111) out-of-plane preferred growth of Pt NPs in the VO₂ matrix. Moreover, the peak positions of VO₂ (020) in all Pt: VO₂ films (≈39.91°) are very close to the bulk VO_2 (020) peak positions ($\approx 39.97^{\circ}$, the black dashed line in Fig. 1a), suggesting no major peak shift for films deposited at different temperatures. The result indicates no obvious strain between the VO₂ matrix and the sapphire substrate, which is possibly due to the incorporation of Pt NPs in the VO₂ matrix. To study the phase transition in Pt: VO₂ films, ϕ -scans by in situ heating XRD of the 500 °C deposited Pt: VO₂ films were performed at room temperature (25 °C) and elevated temperature (90 °C). As shown in Fig. 1b, the low-temperature monoclinic VO₂ (M1) (011) peak was replaced by the tetragonal rutile VO₂ (R) (110) peak at high temperature, confirming the M1-to-R phase transition of the Pt: VO₂ films.

The STEM cross-section images of Pt: VO₂ films deposited at 500, 600, and 650 °C are shown in Fig. 1c2, d2 and e2, respectively. Pt NPs were uniformly distributed in the VO₂ matrix, and a thin layer of Pt was observed in all Pt: VO2 films near the interface of the film and substrate. The Pt layer near the film/substrate interface is very thin (~1 nm) compared to that in the films (~70-80 nm), and could serve as nucleation sites during deposition. All as-deposited films have a similar thickness of around 75 nm. Interestingly, the average Pt NP diameters, as shown in Fig. S2e,† exhibit an obvious increase with the increase in the deposition temperature. The average Pt NP diameters (Fig. S2, the ESI†) were measured as 1.56, 3.36 and 4.26 nm for films deposited at 500, 600, and 650 °C, respectively. The SAED pattern of the film/substrate interface area of the 500 °C deposited Pt: VO2 films, as shown in Fig. S2d,† was recorded from the c-cut sapphire [1010] zone. Orientation relationships of VO₂ (020)//Al₂O₃ (0006) and VO₂ (002)//Al₂O₃ (1210) can be determined from the diffraction pattern, which further confirms the monoclinic structure of VO₂ at room temperature and the highly textured growth of the Pt: VO₂ films. The Pt/V atomic ratio was derived for all Pt: VO₂ films using large-scale EDX mapping data in SEM (Fig. S3, ESI \dagger). The result confirms comparable Pt/V atomic ratio (21 \pm 1%) for all the Pt: VO₂ nanocomposite thin films at deposition temperatures ranging from 500 to 650 °C.

The atomic-scale microstructure of Pt: VO2 thin film deposited at 650 °C was characterized using high resolution STEM (HR-STEM), to investigate the interfacial coupling between Pt NPs and the VO2 matrix. The STEM cross-section image in Fig. 2b shows that Pt NPs were uniformly distributed in the VO₂ matrix. Pt (111) planes are along the out-of-plane orientation, as illustrated in Fig. 2c, suggesting textured growth of Pt (111) in the VO_2 matrix. The result agrees with the XRD θ -2 θ spectrum of Pt:VO₂ film deposited at 650 °C. Since Pt has a face centered cubic structure, VO₂ has a tetragonal rutile structure at deposition temperature and sapphire has a hexagonal structure, Pt NPs tend to have (111) textured growth considering the lattice matching among the Pt NPs, the matrix and the substrate. On the other hand, the Pt (111) out-of-plane preferred growth is also attributed to the lowest surface energy of the Pt (111) plane among all the major Pt surface planes, as reported previously.29 Energy dispersive X-ray spectroscopy (EDS) mapping in Fig. 2d and e confirms the uniform distribution of Pt NPs in the VO2 matrix. Moreover, the interdiffusion between the metal phase and VO2 matrix is restricted. In other words, Pt ad-atoms tend to form NPs on Pt nuclei rather than forming an alloy with the VO2 matrix. The inter-diffusion is limited because of the high thermal stability of the metal phase and the high kinetic energy from the laser system. A weak V signal was detected in areas where Pt NPs were present as shown in Fig. 2d. It was further noted from Fig. 2f that Pt NPs show no obvious oxidation owing to high oxidation resistance of the metal phase.

Nanoscale

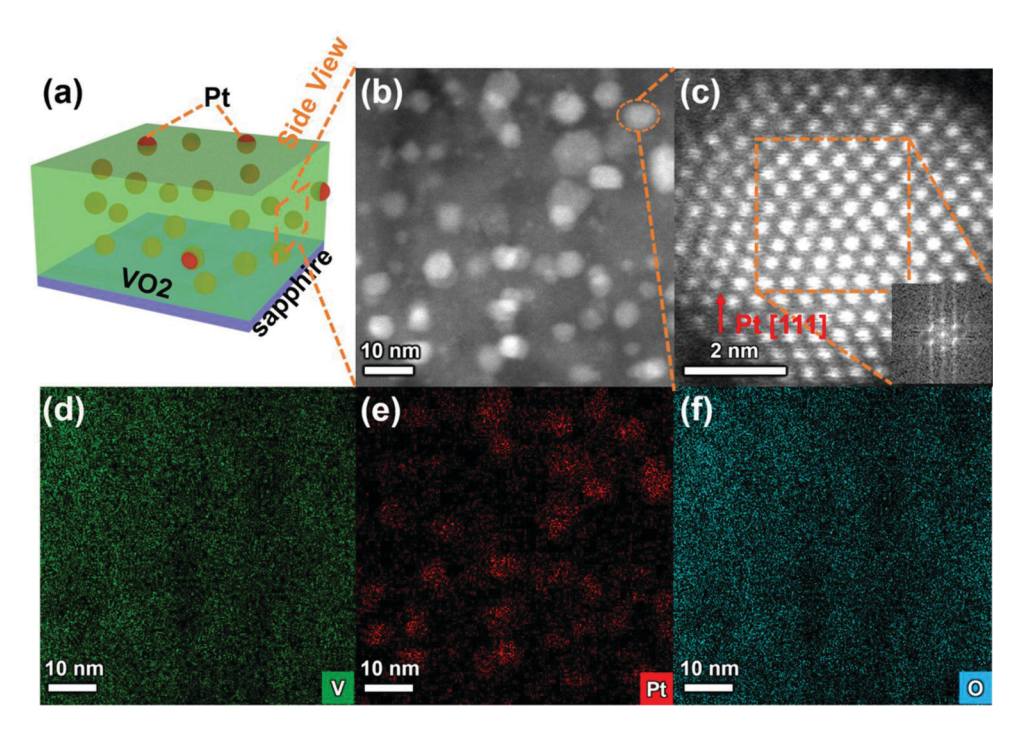


Fig. 2 (a) Schematic diagram and (b) low-magnification STEM cross-section image of 650 °C deposited Pt: VO₂ nanocomposite thin films. (c) Highresolution STEM image of the Pt NP labeled in (b) and its corresponding FFT pattern. (d-f) Cross-section EDS mapping of V, Pt and O elements in the Pt: VO₂ nanocomposite thin films.

The SMT properties of all Pt:VO2 films deposited at different temperatures were characterized by R-T measurements. Fig. 3a shows the normalized electrical resistance, $\rho =$ R(T)/R(390 K), of the pure VO_2 film and $Pt:VO_2$ films as a function of temperature. All SMT parameters in Table 1, including transition temperature (T_c) , transition amplitude (ΔA) , transition sharpness (ΔT) , and the width of thermal hysteresis (ΔH), were calculated and summarized from the derivation of $\log_{10}(\rho)$ versus temperature plot, as shown in Fig. 3b-e. Since the T_c of pure VO_2 films deposited on c-cut sapphire have similar values (345.78 K) in prior work, ²⁷ 500 °C deposited pure VO2 film was used here as a reference. Compared to the pure VO₂ film deposited at 500 °C, the transition curve of the Pt: VO₂ film deposited with the same parameter drastically shifts to the lower temperature, with T_c decreased by 16.56 K to 329.16 K (56.16 °C). In contrast, the transition curve of the Pt: VO2 films deposited at higher temperatures (600 and 650 °C) obviously shifts to the higher temperature end, with T_c increased by 9.55 K to 355.27 K (82.27 °C) and by 15.02 K to 360.74 K (87.74 °C) for Pt: VO2 films deposited at 600 and 650 °C, respectively. As for SMT property comparison, the transition sharpness (ΔT) increases for the Pt:VO₂ film deposited at 500 °C. The broadening of ΔT is related to high defect density at low deposition temperatures.³⁰ In the meantime, both transition amplitude (ΔA) and the width of thermal hysteresis (ΔH) decrease at lower deposition temperatures. The degradation of amplitude is possibly due to the increase of defect content near the grain boundaries,³⁰ while narrower thermal hysteresis is related to lower interfacial

energy and smaller vertical grain boundaries as reported previously.31 Compared to the pure VO₂ film deposited at 500 °C, the Pt: VO₂ film deposited at the same temperature has a significantly lower resistance, indicating much improved film conductivity upon the introduction of Pt NPs. It is also noted that, the Pt: VO₂ film deposited at lower temperatures shows a smaller resistance value, suggesting an improved film charge carrier density due to smaller Pt NPs. Overall, SMT measurements show high quality of Pt: VO2 films with reasonable transition properties compared to the pure VO₂ film.

The bidirectional tuning of T_c with different sizes of Pt NPs is mainly attributed to two factors: the reconstruction of the band structure at the Pt: VO2 interface and the change of the Pt: VO₂ phase boundary density. Initially, the VO₂ matrix forms a Schottky junction upon coming in contact with the metal phase, thereby reconstructing the energy band structure. Though the work function of bulk Pt is ~5.6 eV,32 which is larger than that of VO₂ ~5 eV,³³ the size-dependent work function of Pt NPs can deviate strongly from that of bulk Pt due to the electrostatic interaction with the adjacent VO₂ matrix.^{34,35} Since smaller Pt NPs have larger surface areas when interacting with the matrix, the electrostatic charge transfer at the Pt: VO2 interface is enhanced because of quantum confinement.36,37 As a result, the work function of Pt NPs depends on their charge state, and Pt NPs with smaller size tend to have a reduced work function. 28,38 The lowest work function of Pt NPs is reported to be around 4.6 eV. 39 As shown in scenario a (Fig. 4a1 and a2), the work function of small Pt NPs is lower than that of the VO₂ matrix before contact. When

Paper

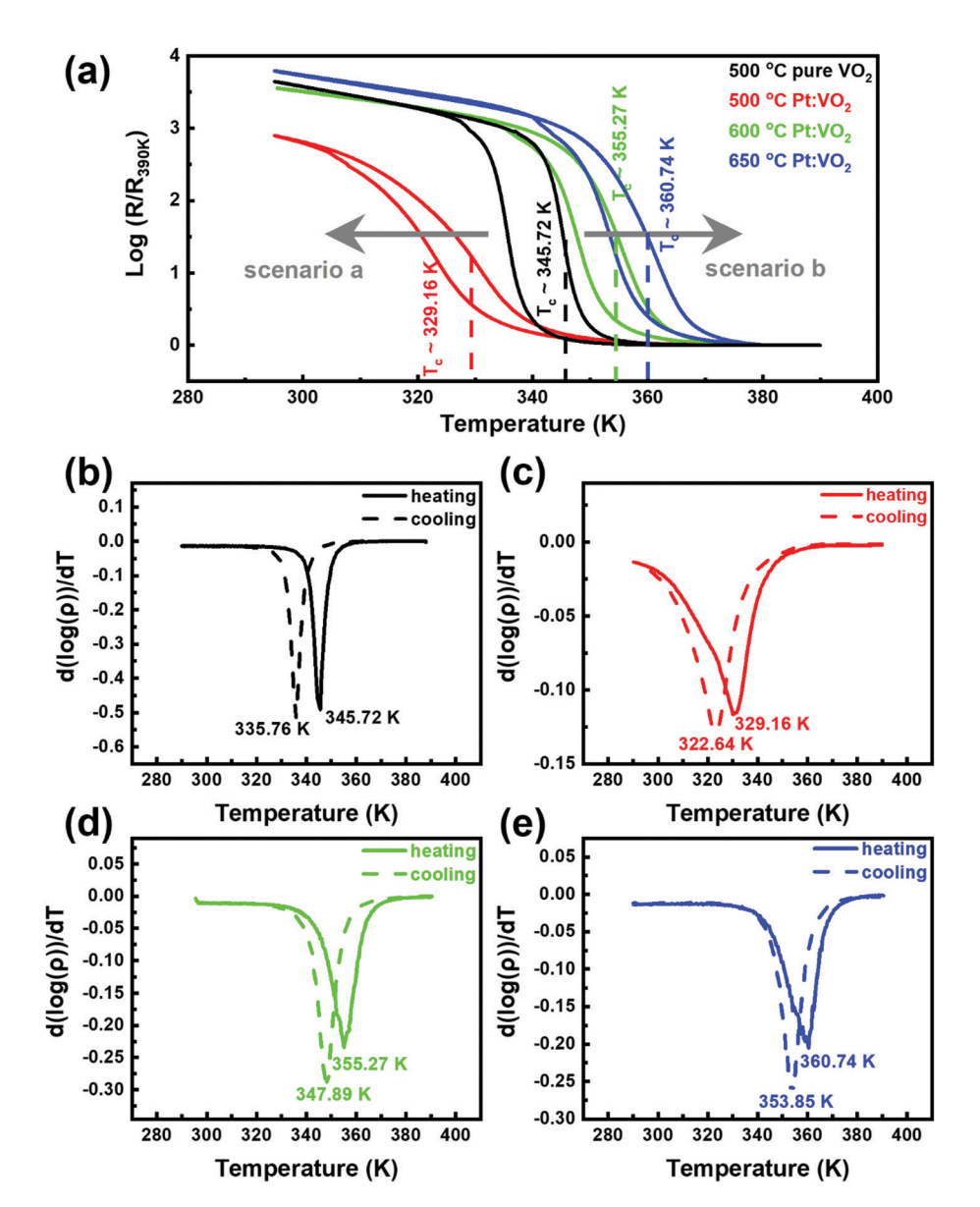


Fig. 3 (a) Normalized resistivity-temperature plots of the Pt: VO₂ nanocomposite thin films deposited at 500, 600, and 650 °C, respectively. (b-e) Resistivity changing rate of pure VO₂ films and Pt: VO₂ films deposited at 500, 600, and 650 °C, respectively.

Table 1 SMT characteristics of the as-deposited pure VO₂ film and Pt: VO₂ films

	Deposition temperature (°C)	$T_{\rm c}\left({ m K}\right)$	ΔA	$\Delta T (K)$	ΔH (K)	$R_{260 \text{ K}} \times 10^4 \Omega$
Pt:VO ₂	500	329.16	6191	12.8	6.52	1.16
	600	355.27	7758	9.7	7.38	3.64
	650	360.74	8765	10.1	6.89	6.33
Pure VO_2	500	345.72	11 759	7.5	9.96	12.25

small Pt NPs and VO2 come in contact, the conduction band of VO₂ bends upward due to the alignment of Fermi levels. Therefore, charge carriers were injected from small Pt NPs into the VO₂ matrix, forming an electron rich region in the VO₂ matrix near the contact interface, which further results in the

drop in T_c by reducing the energy barrier for phase transition. However, in scenario b (Fig. 4b1 and b2), when the work function of large Pt NPs is higher than that of the VO2 matrix before contact, the conduction band of VO2 bends downward when the VO2 matrix comes in contact with large Pt NPs. The consequent charge carrier depletion region in the VO2 matrix near the contact interface will decrease the electron density of the VO_2 matrix and further increase the T_c . The second major factor for bidirectional Tc tuning is the change of Pt NP size and in turn, the variation of the Pt: VO₂ phase boundary density. Smaller NPs tend to have more interface areas with the VO₂ matrix, which cause an increase of overall electron density in the VO2 matrix.27 The increase in the Pt: VO2 phase boundary density with smaller NPs results in a continuous drop of T_c . On the other hand, film strain introduced by the

Nanoscale

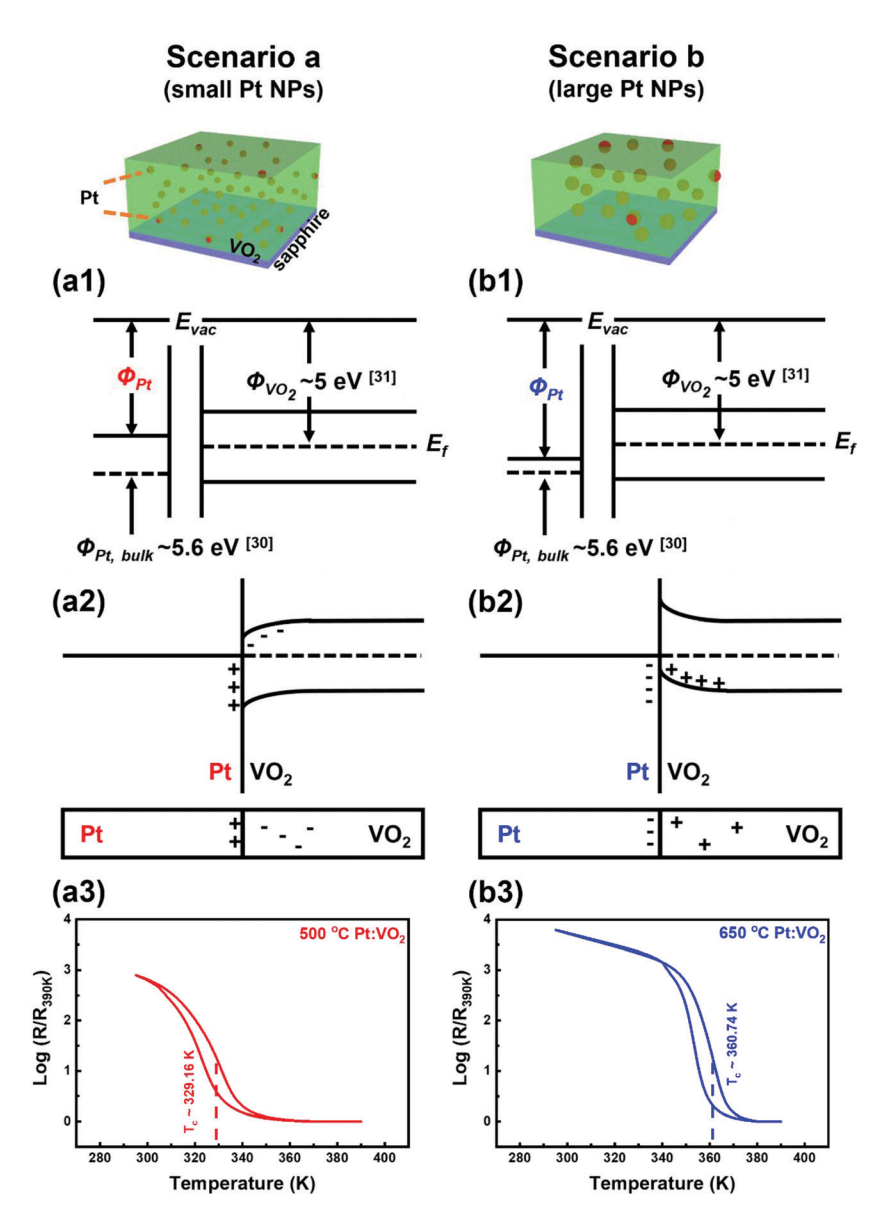


Fig. 4 Band diagram of small Pt NPs and VO₂ (a1) separately, (a2) when forming contacts in scenario a. (a3) Normalized resistivity-temperature plot of the 500 °C deposited Pt: VO2 nanocomposite thin film. Band diagram of large Pt NPs and VO2 (b1) separately (b2) when forming contacts in scenario b. (b3) Normalized resistivity-temperature plot of the 650 °C deposited Pt: VO2 nanocomposite thin film.

film-substrate lattice mismatch could also play a role in the $T_{\rm c}$ change of VO2 films as previously reported. 17-19 Since VO2 (M1) (020) peak in all Pt: VO₂ films shows a very minor shift in the same direction with respect to the pure VO₂ (M1) (020) peak, the strain effect is minimal on the T_c tuning in this case.

Based on the above results, the bidirectional T_c tuning of VO₂ can be effectively achieved by controlling the size of Pt NPs. Small Pt NPs cause an upward band bending of VO2 and a large interface area with VO₂, both leading to the increase of charge carrier density and further drop in T_c . On the other hand, large Pt NPs can result in two competing factors, downward band banding of VO_2 to increase T_c while a small interface area to decrease T_c . The two competing factors thus lead to $T_{\rm c}$ increase with large Pt NPs. The proposed mechanism

also explains the smaller difference in T_c increase than T_c decrease.

Both dielectric permittivities ε' (real part) of Pt:VO₂ films at 25 °C and at 90 °C are plotted in Fig. 5a and b. The dielectric permittivity ε' (imaginary part) is plotted in Fig. S4a and b in the ESI.† The angular dependent spectroscopic ellipsometry measurement assumes an isotropic response of the films. General oscillator models were used in accordance with Kramers-Kronig consistency. A Lorentz model was used for room temperature (25 °C) measurement and a Drude-Lorentz model was used for elevated temperature (90 °C) measurement. The ε' of Pt: VO₂ films remains positive at room temperature, which is consistent with the semiconducting behaviors observed in R-T measurement. At the low frequency Paper Nanoscale

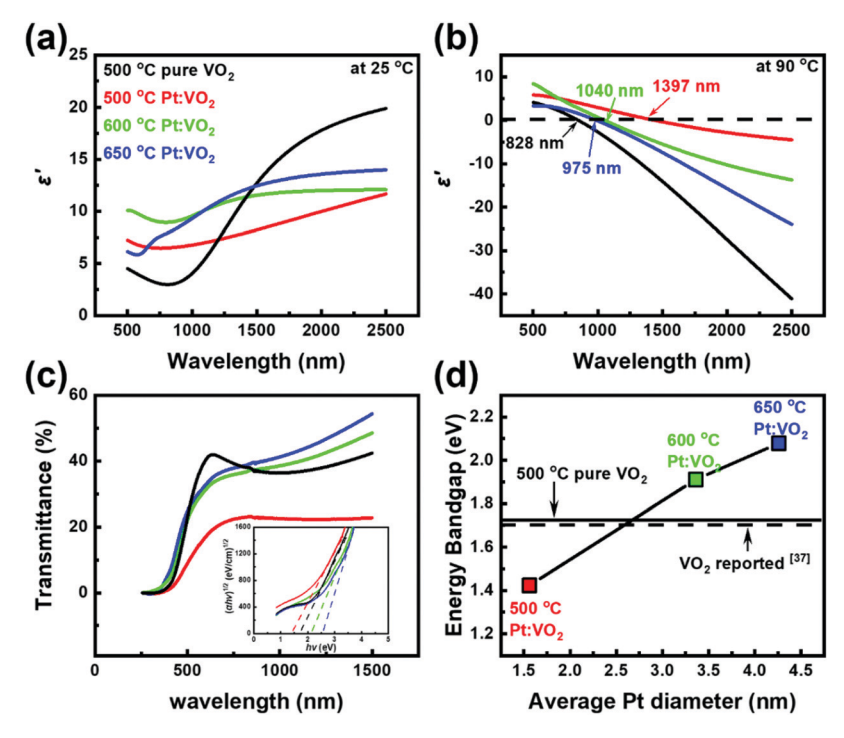


Fig. 5 The real part of dielectric permittivity ε' (a) at 25 °C and (b) at 90 °C of Pt: VO₂ nanocomposite thin films deposited at 500, 600, and 650 °C, respectively. (c) Optical transmittance (T%) spectra of the Pt: VO₂ nanocomposite thin films deposited at 500, 600, and 650 °C, respectively. The inset is the Tauc plot for all Pt: VO₂ films. (d) Tunable energy bandgap of all Pt: VO₂ films as a function of NP size.

(long wavelength) end, the nanocomposite film with small Pt NPs shows a relatively low ε' value, which is also in accordance with high conductivity and high electron density as discussed. On the other hand, Pt: VO2 films behave metallic after phase transition at 90 °C, which is depicted by a negative ε' value in the near-infrared region. Moreover, the size of Pt NPs shows the tunability of the epsilon-near-zero (ENZ) wavelength. The red shift of ENZ wavelength implies the decrease of free carrier density with small Pt NPs after phase transition.

The UV-vis-NIR transmittance spectra of all Pt:VO2 films and pure VO₂ film are shown in Fig. 5c and d. The absorption peak of Pt NPs is not visible due to its high frequency of surface-plasmon resonance (SPR). The corresponding Tauc plot is also shown as an inset in Fig. 5c to calculate the bandgap of VO₂. As shown in Fig. 5d, the bandgap of Pt: VO₂ films varies from 1.42 eV (size of Pt \approx 1.56 nm) to 2.08 eV (size of Pt \approx 4.26 nm). The bandgap of pure VO2 film deposited at 500 °C was plotted as a solid line for reference. The calculated value is comparable to the optical constants available in the literature.⁴⁰ Compared to the pure VO_2 film, the increase and decrease in E_g is in accordance with the energy band structure reconstruction induced by Pt NPs, as illustrated in Fig. 4a1-b1. The upward bending of the VO2 conduction band with small Pt NPs leaves an electron rich region in VO₂ while the downward bending of the VO₂ conduction band with large Pt NPs leaves an electron deficient region in VO₂. The tunability of the bandgap is thus achieved by changing the electron density in the VO₂ matrix.

Taking advantage of the novel Pt: VO2 nanocomposite design, the demonstration of bidirectional T_c tuning provides a

potential candidate for VO₂-based novel electronic and photonic applications operating under specific temperatures. First, compared to the previous metallic doping approach, $^{20-23}$ T_c can be systematically tuned in a broad temperature range via single metal selection in this work. The degradation of phase transition properties at high doping level,24,25 from which the metallic doping approach suffers, is also effectively mitigated by the high quality films via Pt: VO₂ nanocomposite design. Second, the unique Pt: VO₂ nanocomposite film was processed using a single-step PLD method to achieve bidirectional T_c tuning. This is different from the Pt/VO₂ bi-layered films previously reported to achieve a T_c of around 332 K and 345 K depending on the substrate selection and deposition technique. 41,42 Very recently, Jian et al. proposed a combination of metal selection and NP size control to achieve a record low T_c of 301.8 K.²⁷ The novelty of this work lies in that, using tunable metal nanoparticle size, a single metal doping selection can achieve bidirectional T_c tuning over a broad range. As a result of the size dependent work function tunability of Pt NPs, the feasibility of bidirectional T_c tuning was achieved by the Pt: VO₂ nanocomposite design and potentially other metal: VO2 nanocomposites, providing candidates for temperature sensors and thermal switches operating at elevated temperatures.

Conclusions

Bidirectional tuning of the metal-insulator transition temperature (T_c) in VO₂ has been demonstrated via the Pt: VO₂ nanoNanoscale Paper

composite design. Pt NPs were uniformly distributed in the VO₂ matrix, with NP size ranging from 1.56 to 4.26 nm due to the growth temperature variation. T_c is effectively and systematically tuned from 329.16 to 360.74 K as compared to 345.72 K for the pure VO₂ film. Optical properties, including transmittance (T%), dielectric permittivity (ε'), and epsilon-near-zero (ENZ) wavelength were also effectively tuned by the Pt NPs. The mechanism of bidirectional phase transition tuning is mainly attributed to two factors: the reconstruction of the band structure at the Pt: VO2 interface and the change of the Pt: VO₂ phase boundary density. Small Pt NPs bend the VO₂ conduction band upwards and have a large interface area with VO₂, both of which increase the charge carrier density and result in the drop in T_c . On the other hand, large Pt NPs bend the VO₂ conduction band downwards to increase T_c while having a small interface area to decrease T_c , thus partially depleting the charge carrier and causing T_c to increase. This study provides a promising approach towards practical VO2based device applications as novel electronics and photonics under specific operation temperatures.

Conflicts of interest

There are no conflicts to declare.

Acknowledgements

The authors are thankful for the support from the U.S. National Science Foundation: DMR-1809520 for thin film deposition, structural and property characterization studies and DMR-1565822 for high resolution STEM/EDX analysis.

References

- 1 A. Zylbersztejn and N. F. Mott, *Phys. Rev. B: Solid State*, 1975, 11, 4383–4395.
- 2 N. F. Mott, Rev. Mod. Phys., 1968, 40, 677-683.
- 3 M. Cyrot, J. Phys., 1972, 33, 125-134.
- 4 F. J. Morin, Phys. Rev. Lett., 1959, 3, 34.
- 5 J. B. Goodenough, *J. Solid State Chem.*, 1971, 3, 490–500.
- 6 M. Imada, A. Fujimori and Y. Tokura, *Rev. Mod. Phys.*, 1998, **70**, 1039.
- 7 V. Eyert, Ann. Phys., 2002, 11, 650-704.
- 8 P. Miao, J. Wu, Y. Du, Y. Sun and P. Xu, *J. Mater. Chem. C*, 2018, **6**, 10855–10860.
- 9 D. Ruzmetov and S. Ramanathan, *Thin Film Metal-Oxides:* Fundamentals and Applications in Electronics and Energy, 2010, 51–94.
- 10 M. Liu, H. Y. Hwang, H. Tao, A. C. Strikwerda, K. Fan, G. R. Keiser, A. J. Sternbach, K. G. West, S. Kittiwatanakul, J. Lu, S. A. Wolf, F. G. Omenetto, X. Zhang, K. A. Nelson and R. D. Averitt, *Nature*, 2012, 487, 345–348.

- 11 J. J. Yang, M. D. Pickett, X. Li, D. A. A. Ohlberg, D. R. Stewart and R. S. Williams, *Nat. Nanotechnol.*, 2008, 3, 429–433.
- 12 J. Homola, Chem. Rev., 2008, 108, 462-493.
- 13 T. D. Manning, I. P. Parkin, M. E. Pemble, D. Sheel and D. Vernardou, *Chem. Mater.*, 2004, **16**, 744–749.
- 14 E. E. Chain, Appl. Opt., 1991, 30, 2782.
- 15 L. Wang, Y. Yang, J. Zhao, B. Hong, K. Hu, J. Peng, H. Zhang, X. Wen, Z. Luo, X. Li and C. Gao, *J. Appl. Phys.*, 2016, 119, 145301.
- 16 T. H. Yang, R. Aggarwal, A. Gupta, H. Zhou, R. J. Narayan and J. Narayan, J. Appl. Phys., 2010, 107, 053514.
- 17 H. Koo, S. Yoon, O. J. Kwon, K. E. Ko, D. Shin, S. H. Bae, S. H. Chang and C. Park, *J. Mater. Sci.*, 2012, 47, 6397– 6401.
- 18 J. Jian, A. Chen, Y. Chen, X. Zhang and H. Wang, Appl. Phys. Lett., 2017, 111, 153102.
- 19 D. C. Sayle and G. W. Watson, *Phys. Chem. Chem. Phys.*, 2000, 2, 5491–5499.
- 20 N. Wang, S. Liu, X. T. Zeng, S. Magdassi and Y. Long, J. Mater. Chem. C, 2015, 3, 6771.
- 21 B. Chen, D. Yang, P. A. Charpentier and M. Zeman, Sol. Energy Mater. Sol. Cells, 2009, 93, 1550–1554.
- 22 T. D. Manning, I. P. Parkin, C. Blackman and U. Qureshi, J. Mater. Chem., 2005, 15, 4560–4566.
- 23 X. Tan, W. Liu, R. Long, X. Zhang, T. Yao, Q. Liu, Z. Sun, Y. Cao and S. Wei, *J. Phys. Chem. C*, 2016, 120, 28163–28168.
- 24 J. Jian, W. Zhang, C. Jacob, A. Chen, H. Wang and J. Huang, *Appl. Phys. Lett.*, 2015, **107**, 102105.
- 25 L. L. Fan, Y. F. Wu, C. Si, C. W. Zou, Z. M. Qi, L. B. Li, G. Q. Pan and Z. Y. Wu, *Thin Solid Films*, 2012, 520, 6124–6129.
- 26 G. Fu, X. Ning, M. Chen, S. Wang, P. Liu, J. Wang and X. Li, J. Am. Ceram. Soc., 2019, 102, 2761–2769.
- 27 J. Jian, X. Wang, S. Misra, X. Sun, Z. Qi, X. Gao, J. Sun, A. Donohue, D. G. Lin, V. Pol, J. Youngblood, H. Wang, L. Li, J. Huang and H. Wang, Adv. Funct. Mater., 2019, 29, 1903690.
- 28 N. T. Khoa, S. W. Kim, D. H. Yoo, E. J. Kim and S. H. Hahn, *Appl. Catal.*, *A*, 2014, **469**, 159–164.
- 29 L. Vitos, A. V. Ruban, H. L. Skriver and J. Kollár, Surf. Sci., 1998, 411, 186–202.
- 30 J. Narayan and V. M. Bhosle, J. Appl. Phys., 2006, 100, 103524.
- 31 R. Lopez, T. E. Haynes, L. A. Boatner, L. C. Feldman and R. F. Haglund, *Phys. Rev. B: Condens. Matter Mater. Phys.*, 2002, 65, 224113.
- 32 D. Gu, S. K. Dey and P. Majhi, *Appl. Phys. Lett.*, 2006, **89**, 82907.
- 33 C. Ko, Z. Yang and S. Ramanathan, ACS Appl. Mater. Interfaces, 2011, 3, 3396–3401.
- 34 L. Zhou and M. R. Zachariah, *Chem. Phys. Lett.*, 2012, 525–526, 77–81.
- 35 D. M. Wood, Phys. Rev. Lett., 1981, 46, 749.
- 36 L.-S. Li, J. Hu, W. Yang and A. P. Alivisatos, *Nano Lett.*, 2001, 1, 349–351.

Paper Nanoscale

- 37 Y. Zhang, O. Pluchery, L. Caillard, A. F. Lamic-Humblot, S. Casale, Y. J. Chabal and M. Salmeron, *Nano Lett.*, 2015, 15, 51–55.
- 38 H. Zheng, Y. Zhou and S. Gangopadhyay, *J. Appl. Phys.*, 2015, 117, 024504.
- 39 J. K. Schaeffer, L. R. C. Fonseca, S. B. Samavedam, Y. Liang, P. J. Tobin and B. E. White, *Appl. Phys. Lett.*, 2004, 85, 1826–1828.
- 40 S. Y. Li, N. R. Mlyuka, D. Primetzhofer, A. Hallén, G. Possnert, G. A. Niklasson and C. G. Granqvist, *Appl. Phys. Lett.*, 2013, 103, 161907.
- 41 L. Kang, Y. Gao, Z. Chen, J. Du, Z. Zhang and H. Luo, *Sol. Energy Mater. Sol. Cells*, 2010, **94**, 2078–2084.
- 42 J. Sakai, M. Zaghrioui, V. Ta Phuoc, S. Roger, C. Autret-Lambert and K. Okimura, *J. Appl. Phys.*, 2013, 113, 123503.